Modeling Studies of Photoionization Experiments Driven by Z-pinch X-rays

Senior Thesis in Astrophysics

Department of Physics and Astronomy

Swarthmore College

500 College Avenue

Swarthmore, PA 19081

Nathan C. Shupe

nshupe1@swarthmore.edu

February 19, 2005

Advisor: David H. Cohen

ABSTRACT

We have conducted modeling studies of several gas cell shots on the Z accelerator at Sandia National Laboratories in order to study the effects of the irradiance of a low-density gas by a strong x-ray source. Thus far, we have successfully matched a synthesized absorption spectrum to an experimental spectrum obtained from one of the shots, with especially good agreement for many of the absorption lines. Our results have demonstrated we can successfully model the photoionization experiments being conducted at Sandia, and can be used to design new experiments for future shots at Sandia. Our analysis of the excitation/ionization kinematics and physical conditions of the photoionized plasma has also helped benchmark the atomic kinetics models for these plasmas, thereby allowing for better interpretation of measured spectra from plasmas photoionized by cosmic sources.

1. Modeling

Our modeling procedure is a multi-stage simulation process which at each stage uses the results of the previous stage(s) to compute another result. In other words, the result of each simulation (except for the final simulation, since its output is the final result) is used as an input for another simulation. Because each successive simulation is dependent on the simulation(s) that preceded it, this modeling process has a well defined chronological procedure. This procedure is outlined in a flow chart in Fig. 1.1.

There are three main stages of the modeling procedure: [1] compute the incident flux on the face of the gas cell; [2] compute the position and time-depedent temperature and density distributions of the gas in the cell; and [3] synthesize an emission or absorption spectrum. For step [1] we use a 3-D viewfactor code to represent the experimental setup and calculate the radiation field. The values of the albedos for the surfaces are assumed, and the time-dependent pinch radius and power are taken from the experiment. The final result of this step is a time-dependent incident spectrum for a representative surface element of the face of the gas cell. Step [2] inputs the incident flux result of step [1] in addition to EOS and opacity models for all of the gas cell materials, and then performs a hydrodynamics simulation that computes the time-dependent temperature and density distributions of the gas in the cell. This result is used along with the incident spectrum from [1] and detailed atomic level data to synthesize an absorption or emission spectrum in step [3].

The codes implemented for these simulations are [1] *VisRad* (7), a 3-D viewfactor code, [2] *Helios* (4), a 1-D Lagrangian hydrodynamics code, and [3] *Spect3D* (6), a spectral synthesizer. Also employed for these simulations are *AtomicModelBuilder* (3), a program used to create custom atomic models from the ATBASE atomic database, and *Propaceos* (PRism OPACity and Equation Of State) (5), a program that generates equation of state (EOS) and multigroup opacity models.

1.1. VisRad

The first component in our modeling procedure involves calculating the incident flux at the face of the gas cell. For this task we employ the viewfactor code *VisRad* (1). While the gas cell experiments are similar to the x-ray binary system in that the pinch generates a large x-ray flux which can photoionize nearby cool gas, the laboratory experiments differ from the cosmic system in that there are numerous surfaces that can absorb and reemit the radiation emitted by the pinch or reflected by other surfaces. Certainly, in an astrophysical environment, one might approximate the incident flux at a remote location using the inverse square law given by (). In the gas cell experiments, however, this approximation is not a good

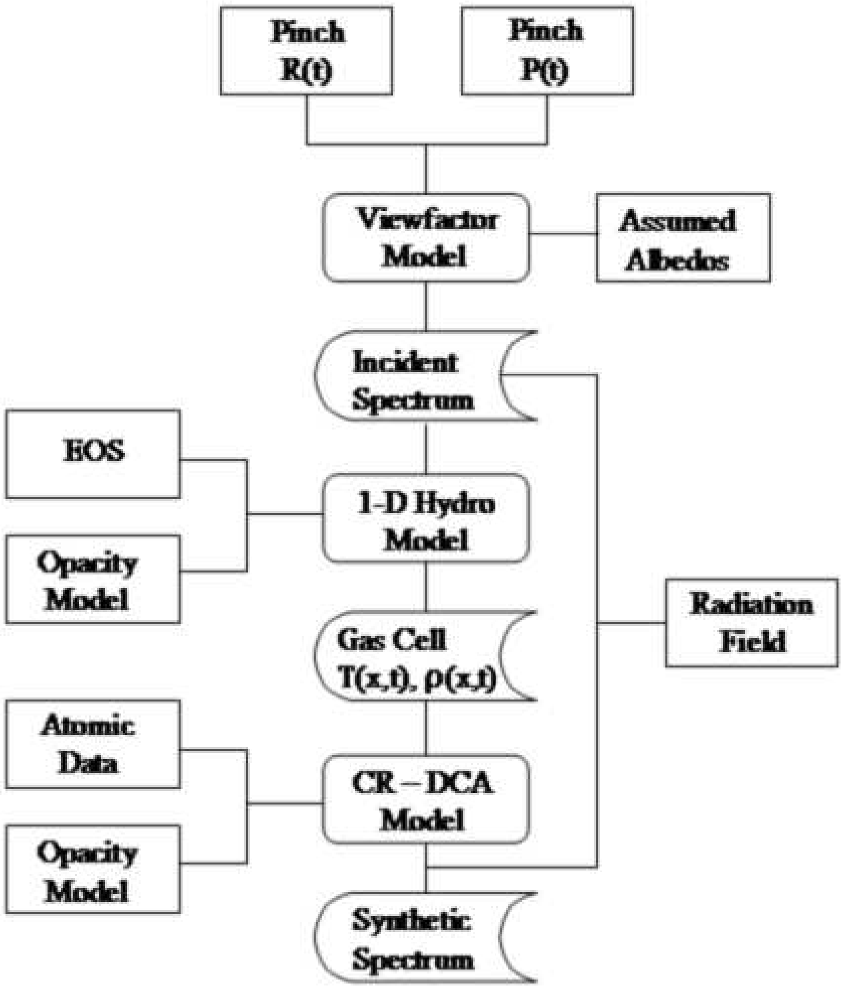

Fig. 1.1.— Flow chart of modeling procedure.

one to make since, as already mentioned, there are many metal surfaces which absorb and reemit radiation. *VisRad* allows us to model all of these metal surfaces, and then calculate the contribution of these surfaces to the incident flux at the face of the gas cell. See Figure 1.2 for a plot of the incident spectra on the center of the gas cell from the different surfaces in the experiment. Notice that the contributions from the surfaces other than the pinch are non-neglible for lower photon energies, which is precisely why it is necessary to use a viewfactor code to calculate the incident spectrum on the gas cell.

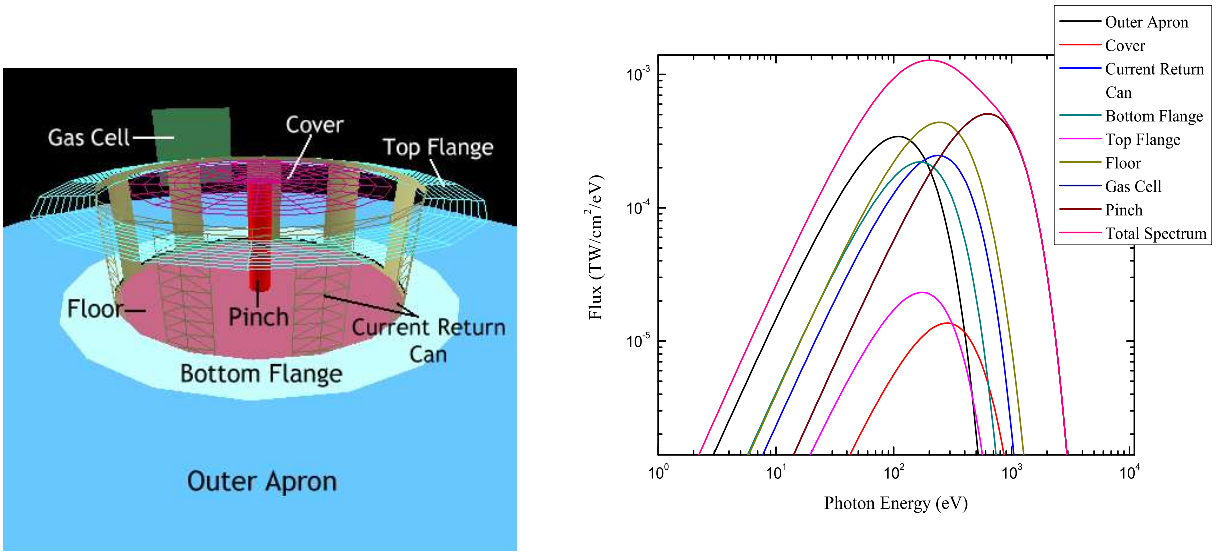

Fig. 1.2.— Contributions to incident spectrum on the center of the gas cell at $t = 100$ ns, the peak of x-ray emission from the pinch. Notice that the pinch contributes the bulk of the high energy incident flux, but also that the contributions of the other surfaces, especially for lower energies, are not neglible.

1.1.1. Constructing a Workspace

Before the incident spectrum on the gas cell can be calculated, however, the experimental setup must first be constructed in the *VisRad* simulation workspace. Similar to how an experimentalist might set up the experiment on the actual Z-machine, the experimental setup is modeled piece by piece by constructing wire-frame structures and applying surface elements to them. For example, the face of the gas cell is modeled as a square wire frame, with 25 surface elements. The square surface elements are the *constituent* pieces of the gas cell, in this case each having $\frac{1}{5}$ the width and height of the total object representing the gas cell. As will be shown in Section 1.1.3, the surface elements are key to computing the incident radiation on the gas cell, since each *viewfactor* is a function between two surface elements. As a result, the number of total surface elements is directly related to the degree of accuracy of the viewfactor simulation. The tradeoff, of course, is that the number of viewfactors increases rapidly as more surface elements are created, thereby causing the computation time to increase as the number of surface elements increases.

The objects are positioned and oriented in a 3-D spatial grid in the same positions and orientations they would have in the actual experiment. Material properties that govern the object's rate of absorption and emission – like albedo (how *reflective* the object is), x-ray conversion efficiency, power, and laser reflectivity (not really useful or important for modeling the gas cell experiments, but a crucial parameter for modeling inertial confinement fusion (ICF) experiments) – can also be specified for the surfaces in the *VisRad* workspace. See Fig. 1.3 for screenshots of the underlying wireframe structure of the workspace objects and the metal surfaces colored by emission temperature for a simulation time just before the peak of the pinch emission and Table 1 for a list of the positions, orientations, dimensions, and material properties of all objects in the *VisRad* model of the gas cell experiment.

1.1.2. Input Parameters

VisRad supports multiple time-step simulations in which dimensions or material properties of objects in the workspace can change with time. The time-dependence of these object parameters can be specified by inputting a table of time-dependent values. It is important to recognize (important enough that this issue will be revisited again in section 1.1.3) that while adding time-dependence to the parameters in the experiment forces the simulation results to be time-dependent, the simulation result for any single time-step is independent of the flux distribution at any other time-step.

In the gas cell experiment, the radius of the pinch decreases as the experiment progresses, so we inputted a time dependent table of values for the radius of the pinch. These time-dependent radial values are plotted in Figure 1.4.

As mentioned earlier, *VisRad* gives the user the option to specify values for the material properties of the object; namely, the albedo, x-ray conversion efficiency, power, and laser reflectivity. Just as we could for the dimensions of the object, we can also make any one of these material properties time dependent by importing a table of times and corresponding property values. For the Z-pinch, the power increases as the radius decreases up until a peak time, and then decreases after the peak. This behavior is shown in Figure 1.5.

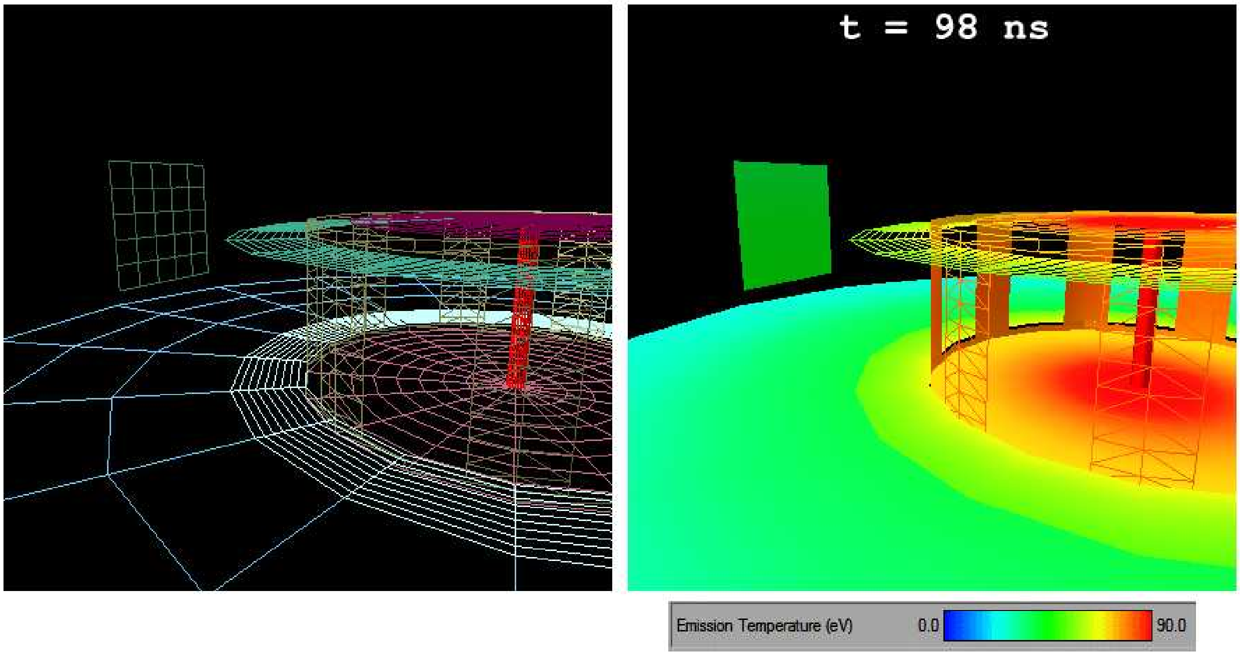

Fig. 1.3.— To the left is a screenshot of the wireframe grid modeling the experimental setup for the gas cell experiment. To the right is a screenshot from the viewfactor simulation, showing emission temperature of the surfaces at a time right before the peak emission of the pinch.

It is important to note that the time-dependent pinch radius and power are not inferred from other quantities or the result of any modeling simulation; rather, these time-dependent pinch data are directly measured in the actual experiment. The radius is measured using a combination of a framing x-ray pinhole camera (FPC) and the Energy-Space-Time (EST) 1-D streaked imager. The power is measured using a filtered x-ray diode array (XRD) in conjunction with a bolometer.(8) The other important parameter in modeling the experiment, i.e. the surface albedos, are not measured directly in the experiment and are instead inferred from the incident spectrum on the gas cell.

Using the time-dependent radial and power data, one can calculate the time-dependent emission temperature of the pinch. In general, we can relate the flux through a unit area on a surface to the luminosity by the equation

$$f = L/A, \tag{1.1}$$

where f is the surface flux, L is the luminosity, and A is the surface area of the radiating object. Now, if we approximate the pinch as a blackbody, we can apply the Stefan-Boltzmann law, which states that the total energy radiated per unit time (i.e. the power) per unit surface

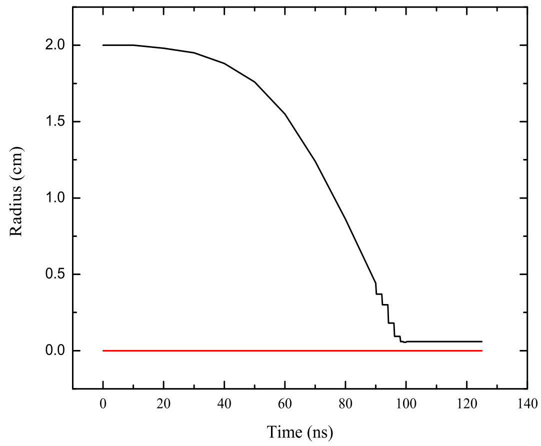

Fig. 1.4.— Time-dependent radius of the pinch. The red line is simply an asymptote at $y = 0$. The jagged feature preceding 100 ns is the result of the interpolation of data points.

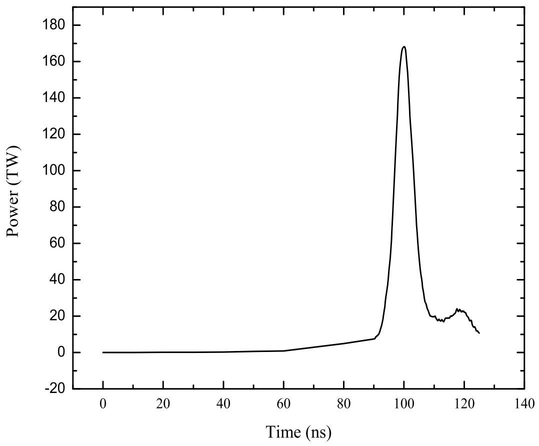

Fig. 1.5.— Time-dependent power of the pinch. Notice that the power of the pinch peaks at approximately 100 ns, and then decreases at a similar rate to its increase before the peak.

area (i.e. the flux) is directly proportional to the fourth power of its temperature, which we will call its emission temperature. Thus,

$$f = \sigma T_{em}^4, \tag{1.2}$$

where the proportionality constant σ is the Stefan-Boltzmann constant. Solving for the flux in either equation, we obtain

$$T_{em} = \left[\frac{L}{A\sigma}\right]^{\frac{1}{4}}. \tag{1.3}$$

Figure 1.6 is a plot of the time-dependent pinch emission temperature.

An interesting feature of the emission temperature plot is the assymmetry about the peak of the emission. On the power plot, the data is very symmetric about the peak at $t = 100$ ns, but on the emission temperature plot there is a shoulder to the right of the peak. At first, one might think that the emission temperature curve behavior should mimic that of the power curve, but (1.3) tells us that for a constant power (i.e. times symmetric about the power peak)

$$T_{em} \propto A^{-\frac{1}{4}} \propto R^{-\frac{1}{4}} \tag{1.4}$$

since if we approximate the pinch as a cylinder, $A = 2\pi Rh$, where R is the radius and h is the height. Thus, if we consider two times symmetric about the pinch power peak, $t = 96$ ns and

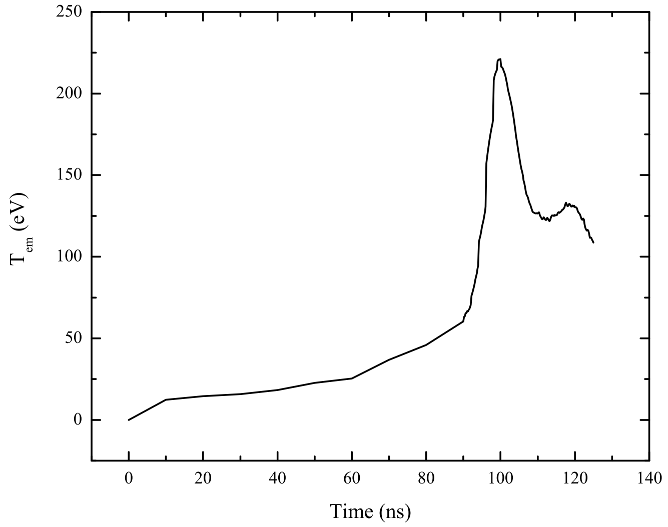

Fig. 1.6.— Time-dependent emission temperature of the pinch.

$t = 104$ ns for example, the power of the pinch at both of those times will be nearly constant, so the emission temperature will depend solely on the radius of the pinch. Since at a later time the pinch radius will be smaller, the emission temperature of the pinch will be higher at that time. This is precisely why there is a shoulder in the pinch emission temperatures for later times, and is also why the emitted flux of the pinch following the peak at $t = 100$ ns is greater than the emitted flux preceding the peak (since according to (1.2) the flux is proportional to the fourth power of the emission temperature).

1.1.3. How does the code work?

As described by MacFarlane (1), the 3-D viewfactor code *VisRad* computes the radiative flux incident on a single surface i element by solving the radiosity equation given by

$$B_i - \alpha_i \sum_j F_{ij} B_j = Q_i, \tag{1.5}$$

where B_i is the emitted flux from surface i (erg s^{-1} cm^{-2}), α_i is the surface albedo, Q_i is the source term, and F_{ij} is the viewfactor between surface i and surface j. The first term on the left, B_i, is the amount of flux emitted by the surface i itself. Using the Stefan-Boltzmann equation (Eq. 1.2), we can convert this flux into an emission temperature, given by

$$T_{em,i} = \left[\frac{B_i}{\sigma}\right]^{\frac{1}{4}}. \tag{1.6}$$

The second term on the left of Eq. 1.5 is the amount of radiated flux from all other surface incident upon surface i that is reflected from surface i. The limits of the albedo coefficient α_i are 1, for a fully reflective surface, and 0, for a fully absorbant surface. The summation adds up the contributions from all other surfaces j by computing for each surface j the viewfactor between surface i and j (the fraction of energy leaving surface j and arriving at surface i, see section 1.1.4) and then multiplying that by the emitted flux of j. Thus, this summation computes the total radiative flux from all other surfaces j incident upon surface i:

$$q_i^{in} = \sum_j F_{ij} B_j, \tag{1.7}$$

where q_i^{in} is the incident flux (erg s^{-1} cm^{-2}). Once again, we can apply Eq. 1.2, and convert this flux to a radiation temperature, given by

$$T_{rad,i} = \left[\frac{q_i^{in}}{\sigma}\right]^{\frac{1}{4}}. \tag{1.8}$$

We are further interested in how the incident flux varies with frequency (i.e. what the incident spectrum on surface i looks like), since the surfaces in the experiment will emit at a wide range of frequencies. Assuming each surface element to emit like a blackbody, the spectrum of each element will be given by the Planck function $B_\nu(T_{em,j})$, where $T_{em,j}$ is the emission temperature of surface j. Now, it can be shown that the Planck function integrated over all frequencies gives

$$\int_0^\infty B_\nu(T_{em,j})\, d\nu = \frac{\sigma T_{em,j}^4}{\pi}, \tag{1.9}$$

which implies that the emitted flux at a single frequency is given by

$$B_j(\nu) = \pi B_\nu(T_{em,j}). \tag{1.10}$$

Substituting this new expression for the radiated flux from surface j in Eq. 1.7, our final expression for the frequency-dependent incident flux on surface i is

$$q_i^{in}(\nu) = \sum_j F_{ij} \pi B_\nu(T_{em,j}). \tag{1.11}$$

Computing the incident flux for each frequency produces an incident spectrum for surface i. Often, we choose the surface element at the center of the gas cell as representative of the

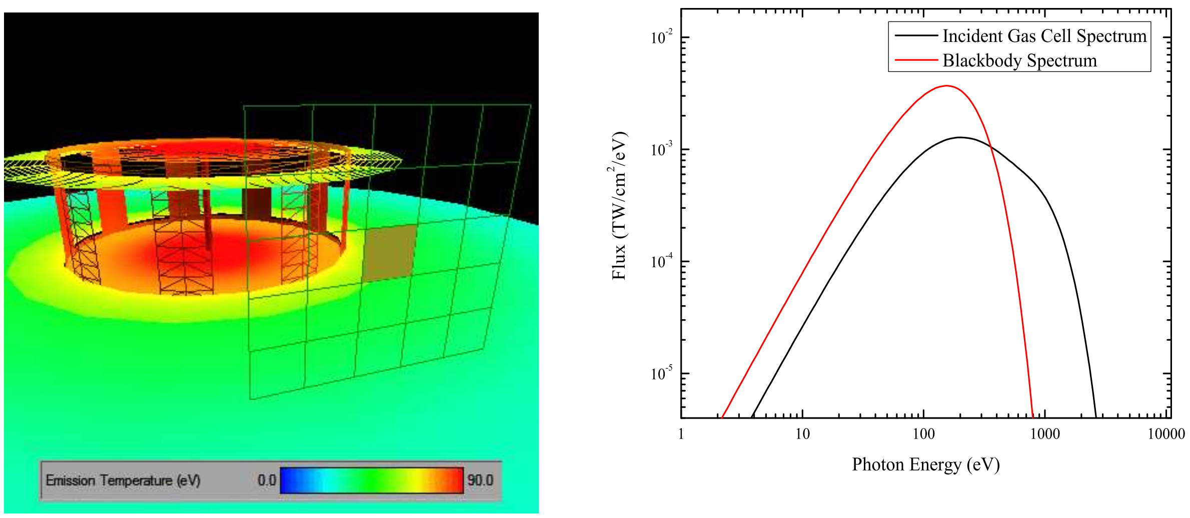

(a) (b)

Fig. 1.7.— (a) *VisRad* screenshot of workspace after the simulation has completed. The highlighted portion of the gas cell is the representative surface element we use to measure the incident spectrum on the gas cell. (b) The spectrum incident upon the highlighted surface element at t = 100 ns and an *equivalent* blackbody of temperature equal to the radiation temperature of the highlighted surface element.

entire face of the gas cell, and output the spectrum incident on that surface. The result is shown in Fig. 1.7.

For each time step in the simulation, *VisRad* recomputes the radiosity balance using Eq. 1.5. This means that the code calculates an emission and radition temperature for every surface element at each time step. To be clear, though, the emission and radiation temperatures calculated at each step are not dependent upon any other time step in the simulation. That is, at each time step, the flux distribution is determined from a coupled set of steady-state power balance equations, and this distribution is independent of the distribution at any other time.

1.1.4. Calculation of Viewfactors

As mentioned in section 1.1.3, the viewfactor between surface i and j is physically the fraction of energy leaving surface i and arriving at surface j. At each time-step of the simulation, *VisRad* recomputes the mutual viewfactor between each surface, so in understanding how *VisRad* computes the incident flux on the face of the gas cell it is crucial that we understand how these viewfactors are calculated. To begin, let us first consider a plane surface, dA_i, which is emitting an intensity of radiation along the surface normal given by I_0. The intensity is related to the flux in the following way (for a blackbody emitter):

$$F(T) = \sigma T^4 = \pi I(T). \tag{1.12}$$

Thus, we can write, using Lambert's Cosine Law (see Fig. 1.9.a):

$$I_{\theta_i} = I_0 \cos\theta_i = \frac{\sigma T^4}{\pi}\cos\theta_i. \tag{1.13}$$

The angular size of the solid angle through which this intensity is emitted at an angle θ_i is given by

$$d\Omega_{\theta_i} = \sin\theta_i d\theta d\phi, \tag{1.14}$$

so the intensity of radiation through the differential solid angle at an angle of θ_i is

$$I_{\theta_i} d\Omega_{\theta_i} = \frac{\sigma T^4}{\pi}\cos\theta_i \sin\theta_i d\theta d\phi. \tag{1.15}$$

The fraction of this intensity that will hit surface dA_j is the ratio of the area of dA_j projected into the plane of the solid angle divided by the area of the solid angle at a distance R_{ij}. The area of dA_j projected into the plane of the solid angle is simply $dA_j \cos\theta_j$ (recall Lambert's Cosine Law), so the ratio of this area to the area of the solid angle at R_{ij} is

$$ratio = \frac{dA_j \cos\theta_j}{R_{ij}^2 \sin\theta_i d\theta d\phi}. \tag{1.16}$$

The product of this ratio of areas and the intensity of radiation (through the solid angle $d\Omega_{\theta_i}$) is the total intensity incident upon surface dA_j from surface dA_i.

$$dI_{ij} = \frac{\sigma T^4 \cos\theta_i \cos\theta_j dA_i dA_j}{\pi R_{ij}^2}. \tag{1.17}$$

Since σT^4 is proportional to the energy emitted by dA_i, then the differential *viewfactor* between surface da_i and surface dA_j is

$$dF_{ij} = \frac{\cos\theta_i \cos\theta_j dA_i dA_j}{\pi R_{ij}^2}. \tag{1.18}$$

VisRad computes the viewfactor between each surface in the workspace by integrating the differential viewfactors over all surface elements of each surface. The result of this integration, F_{ij} is used to calculate the incident flux on each surface element in the workspace.

1.1.5. Spatial variation of incident flux on the face of the gas cell

Since the calculated incident flux on only one surface element of the gas cell is taken as representative of the incident flux hitting the entire face of the gas cell, it is important to investigate the spatial variation of the flux incident on each surface element of the face of the gas cell to ensure this approximation is not an unreasonable one to make. If we take all surface elements of the face of the gas cell to be relatively equidistant from the pinch, then the fraction of the pinch the surface element *sees* will dictate how much flux is incident upon that surface element. Whether a given surface element sees none, a fraction, or the entire pinch is dependent on two factors: (1) the vertical and azimuthal position of the gas cell, and (2) the slot geometry of the current return can. The current return can is a gold cylindrical hohlraum surrounding the pinch through which the *positive* current *returns* to the outer apron after passing through the pinch. In order to allow radiation from the pinch to propagate to the gas cell, holes or *slots* are cut into the current return can. If the position of the gas cell is held constant, then the geometry of these slots (their size and location) completely determines how much of the pinch each gas cell surface element can see. Similarly, once the geometry of the slots in the current return can has been established, then the position of the gas cell becomes critical to determining how much of the pinch different parts of the gas cell can see. If the gas cell is placed too high, the upper portions of the gas cell will have a reduced or no view of the pinch because of obscuration by the top flange and cover. If the gas cell is centered on an azimuthal angle that places it directly behind one of the current return can walls, then only the outer edges of the gas cell will have an unobscured view of the pinch. Shown in Figure 1.10 are the views of the pinch from several different locations on the gas cell. Notice that the surface elements labeled "CENTER" and "SIDE" see the entirety of the pinch, while the surface element labeled "TOP" sees only a fraction of the pinch because part of its view is blocked by the top flange and cover.[1] The partially obscured view of the pinch from the upper surface element of the gas cell is the

---

[1]As you may have noticed, in the *VisRad* screenshot from the "TOP" position the top portions of the pinch are actually visible through the cover and top flange. This is a feature of the *VisRad* program known as *scaffolding* which forces surfaces to be displayed as wire frames if they are obstructing the view of objects behind them along the line of sight of the viewer. While this feature is useful for viewing the workspace in its entirety, for the purposes of the viewfactor simulation all surfaces are solid and have no property of transparency unless specified otherwise.

reason why in Figure 1.8 there is a vertical temperature gradient on the face of the gas cell for peak times in the pinch emission. This gradient is also shown quantitatively in Figure 1.11.

Also included in Figure 1.11 is a plot of the incident spectrum on each of the three representative surface elements at $t = 100$ ns in the viewfactor simulation. Not suprisingly, the flux incident on the "SIDE" and "CENTER" surface elements is nearly the same, whereas the flux on "TOP" surface element is lacking the high energy shoulder that the other two spectra have. As was shown in Figure 1.2 the pinch is the major contributor of the high energy flux at $t = 100$ ns, so it makes sense that the surface element that sees only a fraction of the pinch would receive only a fraction of the high energy flux from the pinch.

This study of the spatial variation of the incident flux on the face of the gas cell demonstrates that given our current placement of the gas cell, a vertical temperature gradient appears at the peak of the pinch emission due to the partial obscuration of the view of the pinch from the upper portions of the gas cell. It is unclear how pronounced an effect this temperature gradient might have on the emission and absorption spectra we measure, but is certainly something to keep in mind if discrepancies between the synthesized and experimental spectra appear.

1.2. Helios

In the gas cell experiments, a sample of gas initially at a low temperature and uniform density is bombarded on one side by a large high energy flux. The rapid non-uniform heating that results from this asymmetric energy flux bombardment gives rise to hydrodynamic motion of the gas in the cell in the form of shock and compressional heating. If we are to synthesize an accurate absorption and/or emission spectrum for the gas in the cell, it becomes vital for these experiments to know how the temperature and density distributions of the gas as in the cell change with time, since these distributions will directly effect how radiation is transfered by the gas.

The code employed to calculate the hydrodynamic motions (ultimately calculating time-dependent temperature and density distributions) of the gas in the cell of these experiments is *Helios* (2), a one-dimensional radiation-magnetohydrodynamics code that models the dynamic evolution of high energy plasma. For the purposes of this investigation, the *magnetohydrodynamic* feature of this code is not used, but magnetic fields become much more important when modeling coronal plasmas in objects like the Sun.

As discussed in detail by MacFarlane et al. in (2), *Helios* solves a series of partial differential equations in order to calculate the time-dependent temperature and density distributions. These equations are derived from conservation considerations, and are as follows:

Mass Conservation

In a Lagrangian hydrodynamic system, the mass of each volume element is conserved because the spatial grid moves with the mass. In this system, the mass of each volume element is given by

$$dm_0 = \rho(r) r^{\delta-1} dr, \tag{1.19}$$

where ρ is the mass density, r is the spatial coordinate, and $\delta = 1$ for the planar geometry of the gas cell. The mass conservation criterion can then be expressed explicitly as

$$\frac{\partial V(r)}{\partial t} = \frac{\partial}{\partial m}(r^{\delta-1}u), \tag{1.20}$$

where $V(r)$ is the specific volume, ρ^{-1}, in units of (cm g^{-1}), and u is the fluid velocity in units of (cm s^{-1}). This equation says that the rate of change of the volume per unit mass is equal to the derivative (with respect to the mass) of the rate at which the mass is moving (since the spatial coordinate goes to 1 for $\delta = 1$). Essentially, this means that the rate of the change of the specific volume (the volume per unit mass) at a certain radius must equal the rate at which mass is leaving (or arriving) at that radius. One might think of this as the specific volume *stretching* to accomodate new mass and *compressing* to compensate for lost mass. As expected, this implies that the the spatial grid *moves* with the mass in this system.

Momentum Conservation

If we approximate the flow of the plasma as a single fluid (electrons and ions flow together at the same rate), then the equation of momentum conservation is

$$\frac{\partial u}{\partial t} = -r^{\delta-1}\frac{\partial}{\partial m_0}(P_e + P_i + P_r + q) \tag{1.21}$$

where P_e, P_i, P_r are the electron, ion, and radiation pressures respectively, and q is known as the Von Neumann artificial viscosity. If we think of pressure as an energy density, having units of (erg cm^{-2}) for a planar geometry, then the derivative with respect to mass has units of force per unit mass, or acceleration (cm s^{-2}), which as expected matches the units of the derivative of the fluid velocity on the left. This equation, therefore, is merely a restatement of Newton's second law, $F = ma$, where the left side of the equation is the acceleration and the right side is the force scaled by the mass (since the pressure for a planar geometry is simply the force scaled by the spatial coordinate).

The Von Neumann artificial viscosity term is included to effectively *smooth* shocks by spreading out a rapid increase in pressure over a small number of zones (rather than having a discontinuous pressure increase over a single zone).

Energy Conservation

The equations of energy conservation, written in terms of temperature diffusion equations (for a two temperature model for the electrons and ions) are given by

$$C_{v,e}\frac{\partial T_e}{\partial t} = \frac{\partial}{\partial m}\left(r^{\delta-1}\xi_e\frac{\partial T_e}{\partial r}\right) - \omega_{ei}\left(T_e - T_i\right) - \left[\frac{\partial E_e}{\partial V} + P_e\right]\frac{\partial V}{\partial t}T_e + R_{Abs} - R_{Emis} + \Psi + S_e \tag{1.22}$$

and

$$C_{v,i}\frac{\partial T_i}{\partial t} = \frac{\partial}{\partial m}\left(r^{\delta-1}\xi_i\frac{\partial T_i}{\partial r}\right) + \omega_{ei}\left(T_e - T_i\right) - \left[\frac{\partial E_i}{\partial V} + P_i\right]\frac{\partial V}{\partial t}T_i - q\frac{\partial V}{\partial t} \tag{1.23}$$

where T is the temperature ($\circ$ K), C_v is the specific heat capacity (erg $\circ$K^{-1} g^{-1}), ξ is the thermal conductivity (erg s^{-1} cm^{-1} $\circ$ K), E is the specific internal energy (erg g^{-1})...

As inputs for this calculation, equation of state (EOS) and opacity databases...

1.2.1. Propaceos

1.2.2. Ion Temperature and Mass Density Output

1.2.3. Non-LTE vs. LTE

In general, a closed system is said to be in *thermodynamic* or *thermal equilibrium* if there is no net flow of energy through that system. As an example, consider a box filled with gas. If we think of this system as containing both gas particles and radiation (in the form of photons), then our requirement for thermodynamic equilibrium is that there is no net flow of energy between the particles, and no net flow between the gas particles and the ambient radiation field in the box. The most simple example of such a system would be one at absolute zero, where the particles are not moving and are not emitting any radiation (since they have no energy). It is possible, however, to achieve thermal equilibrium for a temperature other than absolute zero, as long as you thermally insulate or close the system. In such a system, the temperature is held uniform because every process that could change the energy distribution, like the emission of a photon, is balanced by its inverse process, in this case the absorption of a photon. This process/inverse process balance is also true for the particles themselves. For a given uniform gas temperature the particles are characterized by a specific distribution of velocities known as the Maxwell-Boltzmann distribution. Now, for any collision in which the kinetic energies of any particles pair are changed, there is another collision of a second pair of particles of initial kinetic energies equal to the final kinetic energies of the first pair which results in second pair having kinetic energies equal to the initial kinetic energies of the first pair. In other words, collisions occur and energy is transferred between particles, but overall for the system the velocity (or energy, since $KE = \frac{1}{2}mv^2$) distribution is conserved for a system in thermal equilibrium.

Of course, closed systems in thermodynamic equilibrium are idealizations of the truth, because practically speaking it is never possible to fully isolate a system from its surroundings. Though, we can approximate a condition of thermal equilibrium for a system if the distance over which the temperature changes is large compared to the distance over which a particle or photon collides with another particle (known as the *mean free path*). This approximate condition of thermal equilibrium is known as *local thermodynamic equilibrium* (LTE), and is a valid approximation for a region of nearly constant temperature in which the photons and particles contained in the system cannot escape (because they collide with another particle first).

Relevant to our investigation is the determination of whether the gas in the cell is in LTE. Certainly, it would seem that as long as the gas in the cell is bombarded from one side by a high energy density flux, there will be a non-zero net flow of energy through the system (since the temperature of the gas closest to the pinch will be higher than the temperature of the gas farther from the pinch). It is possible that the net flow of energy will tend toward zero both for early times when the pinch emission is neglible and for late times when the pinch has turned "off" after its peak emission, but the features (absorption and emission) for a time-integrated spectrum will be dominated by the state of the gas at the peak of the pinch emission rather than early or late pinch emission at the beginning or end of the experiment respectively. Thus, in trying to accurately model the hydrodynamic evolution of the gas in the cell, we are much more concerned with what the gas is doing at or around the peak pinch emission than we are with what it is doing at then end (or beginning) of the experiment.

Assuming that the part of the experiment in which we are most interested is not well approximated by LTE, it then becomes necessary to track the atomic rate equations at each time step of the simulation. For a uniform electron temperature set by LTE, the level populations are set by the Boltzmann (for excited states) and Saha (for ionization states) equations. However, for our case where the temperature is not uniform over a distance significantly larger than the mean free path, there is not a single temperature we can use to calculate the level populations from the Saha and Boltzmann equations. Instead, for a non-LTE calculation, *Helios* calculates the level populations at each time step by solving a set of multi-level atomic rate equations. This modification can make a significant difference in the calculated temperature distribution, as shown in Fig. 1.12.

1.3. Spect3D

1.3.1. Atomic Model Builder

1.3.2. Absorption and Emission Spectra

REFERENCES

J. J. MacFarlane. VISRAD-A 3-D view factor code and design tool for high-energy density physics experiments. *Journal of Quantitative Spectroscopy and Radiative Transfer*, 81:287–300, September 2003.

J. J. MacFarlane, I. E. Golovkin, and P. R. Woodruff. Helios-cr - a 1-d radiation-magnetohydrodynamics code with inline atomic kinetics modeling. Technical report, Prism Computational Sciences, Inc., 2005?

Prism Computational Sciences, Inc. *AtomicModelBuilder*, 2.6.0 edition. [http://www.prism-cs.com/Software/AtomicData/AtomicModelBuilder.htm].

Prism Computational Sciences, Inc. *HELIOS*, 2.1.0 edition. [http://www.prism-cs.com/Software/Helios/Helios.htm].

Prism Computational Sciences, Inc. *PROPACEOS*, 2.0.0 edition. [http://www.prism-cs.com/Software/PROPACEOS/PROPACEOS.htm].

Prism Computational Sciences, Inc. *SPECT3D*, 4.1.0 edition. [http://www.prism-cs.com/Software/Spect3D/Spect3D.htm].

Prism Computational Sciences, Inc. *VISRAD*, 4.0.0 edition. [http://www.prism-cs.com/Software/VisRad/VisRad.htm].

G. A. Rochau. *Radiative Transfer in Low-Density, Low-Z Foam.* PhD thesis, University of Wisconsin - Madison, 2003.

This preprint was prepared with the AAS LATEX macros v5.0.

Table 1: VisRad Simulation Parameters

OBJECT	Outer Apron	Cover	Current Return Can	Bottom Flange	Top Flange	Floor	Gas Cell	Pinch
POSITION								
r (cm)	0	0	0	0	0	0	5.65	0
z (cm)	-0.85	1	0	-0.85	0.85	-1.0	0.77	0
phi(deg)	0	0	0	0	0	0	0	0
polar	0	0	0	0	0	0	90	0
azimuthal	0	0	0	0	0	0	0	0
rotation	0	0	0	0	0	0	0	0
SIZE/ GRIDDING								
size (cm)	$r_{min} = 3.32$ $r_{max} = 7.0$	$r_{min} = 0$ $r_{max} = 2.0$	$r = 2.5$ $h = 2.0$	$r_{min} = 2.5$ $r_{max} = 3.32$	$r_{min} = 2.5$ $r_{max} = 3.32$	$r_{min} = 0$ $r_{max} = 2.5$	$l = 2.0$ $w = 2.0$	r varies $h = 1.98$
min. angle	0	0	0	0	0	0	...	0
max. angle	360	360	360	360	360	360	...	360
radial grid points	4	10	10	10	10	10	6	10
azimuthal grid points	18	18	18	18	18	18	6	18
surface normals	up	down	in	up	down	up	down	out
MATERIAL PROPERTIES								
albedo	variable	variable	variable	variable	variable	variable	0.5	0.7
power (TW)	0	0	0	0	0	0	0	variable

Table 2: Helios Simulation Parameters

SPATIAL GRID									
Region	R_{min}	R_{max}	DCA Material	Thickness	Mass Density	Number of Zones	Mean Atomic Weight	Temperature	Velocity
	(cm)	(cm)		(cm)	(g/cc)		(amu)	(eV)	(cm/s)
mylar1	0.0	0.00014	no	0.00014	1.39	20	8.735	0.025	0.0
neon	0.00014	1.10014	yes	1.1	3.6×10^{-5}	20	20.18	0.025	0.0
mylar2	1.10014	1.10028	no	0.00014	1.39	20	8.735	0.025	0.0

ATOMIC PROCESSES (Non-LTE)						
Collisional Excitation/ Deexcitation	Spontaneous Emission	Photoexcitation/ Stimulated Emission	Radiative Recombination	Collisional Ionization/ Recombination	Autoionization/ Dielectronic Recombination	Photoionization/ Stimulated Recombination

OTHER SETTINGS					
Minimum Temperature for CR (eV)	Points in Continuum	Additional Points Per Line Transition	Radiation Transport Model	Frequency Groups	Energy Model
10	200	15	Multiangle (2)	50	$T_i = T_e$

Table 3: Spect3D Simulation Parameters

MATERIALS					
	DCA Material	Mean Atomic Weight (amu)	Element Number	Element Symbol	Number Fraction
mylar	yes	8.735	1	H	0.364
			6	C	0.455
			8	O	0.182
neon	yes	20.18	10	Ne	1.00

KINETICS MODEL				
DCA Level Population Model	Photoexcitation Model	Photoionization Model	Points in Continuum	Additional Points Per Line Transition
Collisional-Radiative	Non-Local Radiation Radiation (1-D Planar or Spherical)	Non-Local Radiation Radiation (1-D Planar or Spherical)	200	15

DETECTOR													
Position (cm)			Center of Projection (cm)			Pixel Count		Pixel Spacing		Projection	Vertical Alignment	XRD Resistance (ohms)
X	Y	Z	X	Y	Z	HORIZ.	VERT.	HORIZ.	VERT.	Orthographic	Z-Axis	50
1.0	1.0	1.0	0.0	0.0	0.0	1.0	1.0	0.05	0.05			

OTHER SETTINGS				
Hydrocode File Type	CR Simulation Type	Geometry	Plasma Grid Type	Backlighter Spectral Type
EXODUS	Steady-State	1-D	Absolute (Lagrangian)	Continuum T = 500 eV

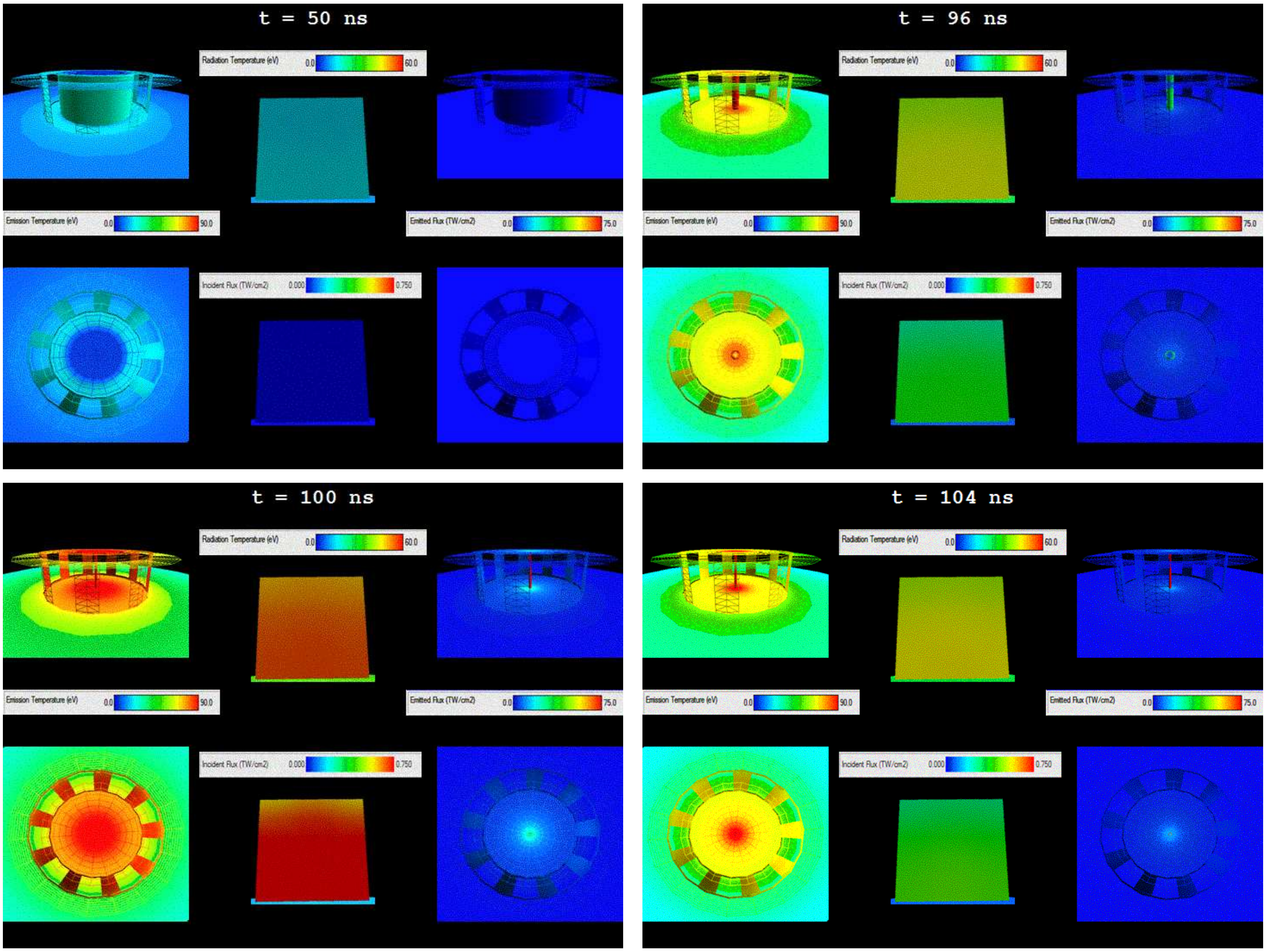

Fig. 1.8.— Compiled snapshots of the *VisRad* simulation for different times. In each snapshot, the gas cell is pictured in the middle column, and the pinch and diode assembly are pictured in the left and right columns.

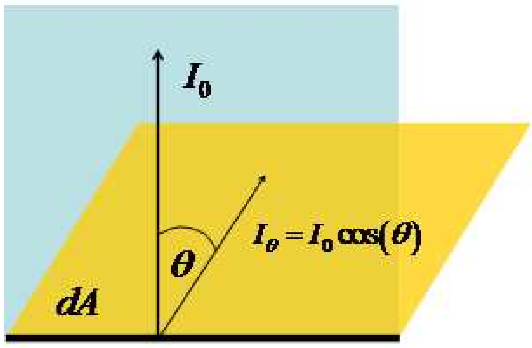

(a)

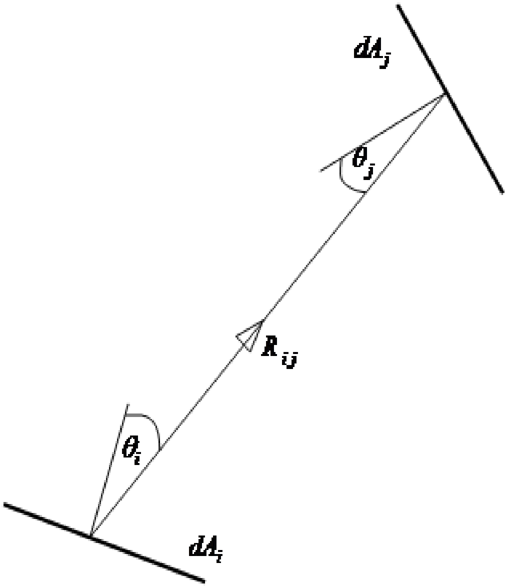

(b)

Fig. 1.9.— (a) Diagram of Lambert's Cosine Law. This law simply says that the amount of radiation an observer receives is proportional to the ratio of the amount of surface area the observer can see to the total surface area. (b) Diagram showing the parameters necessary for computing the viewfactor between two surfaces elements.

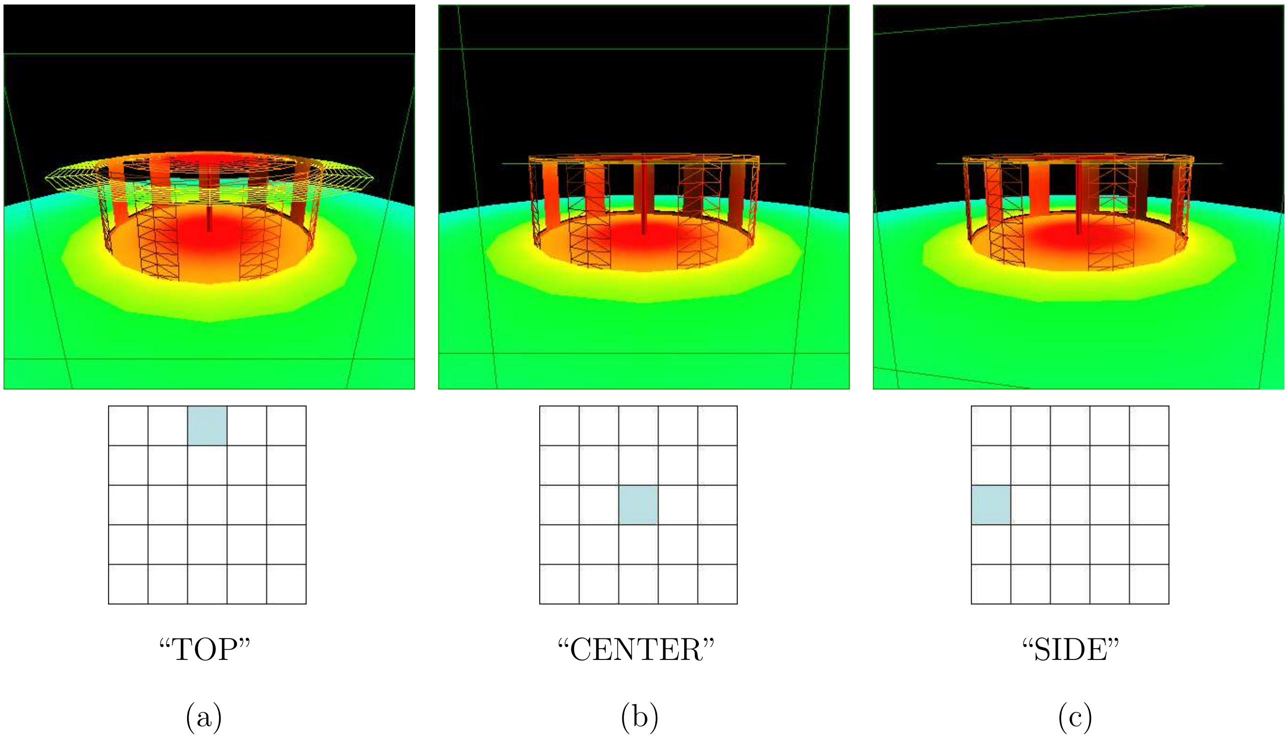

Fig. 1.10.— Views of the pinch from surface elements located at the (a) TOP, (b) CENTER, and (c) SIDE of the gas cell. In each column, the top image is a screenshot captured from a viewing position directly behind the relevant surface element of the gas cell. The relevant surface element for each column is highlighted in blue in the diagram immediately below the *VisRad* screenshot.

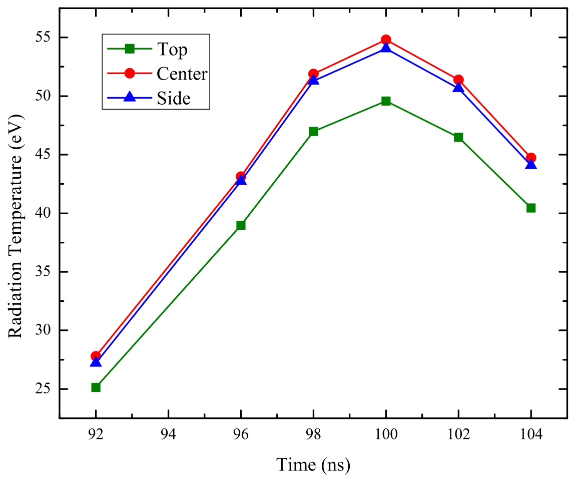

(a)

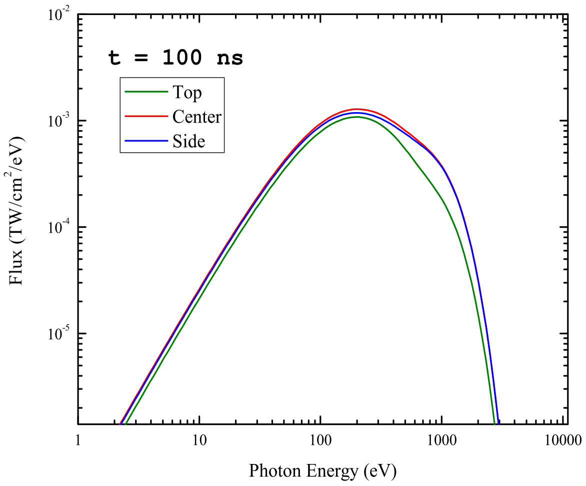

(b)

Fig. 1.11.— (a) Time-dependent radiation temperature of three representative surface elements of the face of the gas cell, and (b) the incident spectrum on each of these surface elements at $t = 100$ ns.

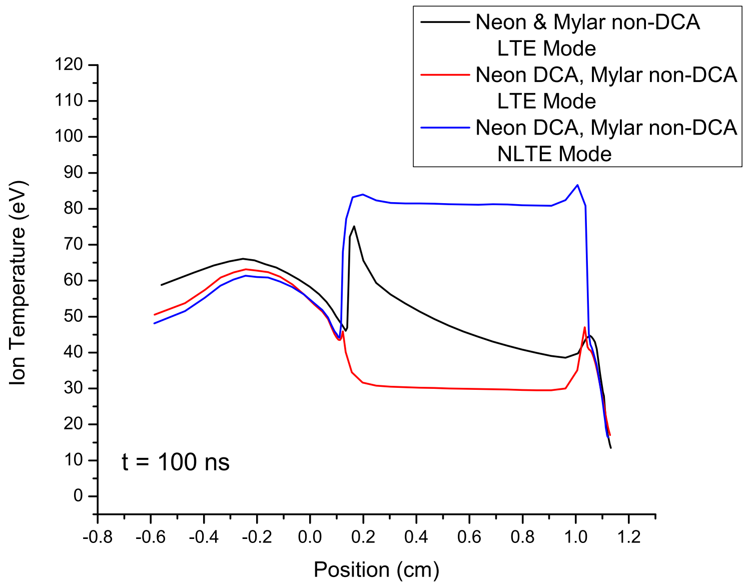

Fig. 1.12.— Comparison of ion temperature distributions at $t = 100$ ns for three independent simulations. Notice that in non-LTE mode, *Helios* calculates a higher average ion temperature at the peak of the pinch emission. The DCA label (Detailed Configuration Accounting) for each material in the simulation refers to how the opacities of each material are calculated. If a material is labeled as non-DCA, then multigroup opacities are used from a *Propaceos* data table. Otherwise, if a material is labeled as DCA, then frequency-dependent opacities are calculated based on the atomic level populations at each time-step. These populations can be calculated using either a LTE or a non-LTE model.